Enhancing Voltage Control Stability of Grid-Forming VSCs Under PWM Delays: A Study on Feedforward Damping Methods

He, Shan; Gao, Chao; Yang, Zhiqing; Li, Helong; Ding, Lijian; Blaabjerg, Frede

Published in:
I E E E Transactions on Circuits and Systems Part 1: Regular Papers

DOI (link to publication from Publisher):
10.1109/TCSI.2024.3523196

Publication date:
2025

Document Version
Accepted author manuscript, peer reviewed version

Enhancing Voltage Control Stability of Grid-Forming VSCs Under PWM Delays: A Study on Feedforward Damping Methods

Shan He, *Senior Member*, *IEEE*, Chao Gao, Zhiqing Yang, *Member*, *IEEE*, Helong Li, *Senior Member*, *IEEE*, Lijian Ding, *Member*, *IEEE*, and Frede Blaabjerg, *Fellow*, *IEEE*

***Abstract*—Grid-forming converters have demonstrated their ability to enhance the operation of renewable energy resources by providing essential grid voltage and frequency support. However, control delays can cause the output impedance of the converter having a negative-resistance region, which potentially leads to high-frequency instability in voltage control. While passivity-based design is typically employed to shape the output impedance, aspects such as ease of implementation, robustness, and constraints related to *LC*-filter design have not been fully explored. To address this gap, this paper examines four feedforward damping methods with varying sampling rates, ultimately recommending sixteen-sampling capacitor voltage feedforward as the optimal approach. The effectiveness of proposed approach is validated through experiments, with grid current feedforward used as a benchmark for comparison.**

***Index Terms*—Voltage control, feedforward, sampling rates, harmonic stability, impedance shaping.**

I. Introduction

Grid-forming voltage source converter (VSC) are increasingly vital in power systems that incorporate a large proportion of renewable energy, especially as traditional grid-following VSCs face limitations [1]. Grid-following VSCs rely on a stable grid for synchronization, making them susceptible to instability in weak grids or scenarios with low inertia [2]. In contrast, grid-forming VSCs emulate the behavior of synchronous machines, independently establishing and regulating grid voltage and frequency [3]. This capability is crucial for stabilizing weak grids, supporting islanded operation, and ensuring the seamless integration of renewable energy sources while maintaining overall grid resilience [4-5].

The stability and control of grid-forming converters are crucial aspects of their operation. Typically, harmonic instability can arise from the inner voltage control loop due to delays inherent in the pulse width modulation (PWM) process [6]. Additionally, the outer synchronization loops, such as the power control loop and the DC-link voltage loop, can lead to low-frequency instability. This is because their bandwidth is intentionally designed to be much lower in order to decouple their dynamics from those of the inner voltage control loop [7].

This paper emphasizes the design of damping for voltage control, with the dynamics of outer loops being neglected. Frequency domain passivity theory has become a valuable method for analyzing and ensuring the stability of grid-forming converters [8-9]. The theory suggests modeling a grid forming VSC as a controlled voltage source together with an output impedance connected in series. To ensure stable operations, both internal and external stability shall be carefully designed. First, the internal stability must be ensured by stabilizing the controlled voltage source, which is determined by the transfer function linking the reference voltage and the output voltage. Second, the external stability should also be enhanced by reshaping the converter output impedance towards passive in the desired frequency range, so that stable interactions of the VSC and grid can be guaranteed.

During the initial stage, the internal stability regarding the controlled voltage source was mainly considered. It has been found that the conventional proportional-resonant (PR) voltage controller can limit the control bandwidth and the *LC*-filter design [10]. Moreover, these two limitations can be released by modifying the PR controller, i.e., setting the P gain to be negative or zero [11-12]. By further considering the outer loop, the voltage controller is optimized with fast dynamics and less overshoot [13-14]. However, these methods often overlook the analysis of high-frequency external stability with the grid.

On the other hand, passivity-based damping design is mainly used to shape the converter output impedance, where the phase characteristic is within $[-90^\circ, 90^\circ]$ or the real part is non-negative [8]. Due to the control delay in the PWM process, the positive-resistance (or called dissipative) region is usually limited leading a risk of instability. Grid current feedforward is commonly used for dissipativity enhancement where the phase of converter output impedance is set to 90° at the critical frequency [9]. However, the system robustness to parameter variations in terms of dissipativity is limited. Moreover, this method requires extra current sensors, which leads to higher cost [9, 15-16]. Capacitor voltage feedforward has simple

This work was supported in part by the Reliable Power Electronics-Based Power System (REPEPS) project funded by Villum Foundation, and partly supported by National Natural Science Foundation of China under Grant 52407199. (*Corresponding author*: *Zhiqing Yang*)

Shan He and Frede Blaabjerg are with Department of Energy, Aalborg University, Aalborg 9220, Denmark (e-mail: shanhe@ieee.org, fbl@energy.aau.dk).

Chao Gao is with the Department of Electronic Engineering, the Chinese University of Hong Kong, Hong Kong, China (e-mail: chaogao@link.cuhk.edu.hk).

Zhiqing Yang, Helong Li, and Lijian Ding are with the State Key Laboratory of High-Efficiency and High-Quality Conversion for Electric Power (Hefei University of Technology), Hefei 230009, China, and Institute of Energy, Hefei Comprehensive National Science Center (Anhui Province Energy Laboratory), Hefei 230031 (e-mail: zhiqing.yang@hfut.edu.cn; helong.li@hfut.edu.cn; ljdin@hfut.edu.cn).

implementation, which is equivalent to negative P-gain control, but its positive-resistance region is limited [17]. Additionally, a state-space-based damping method is proposed in [18], but it involves complex control with five states in the feedforward. In [19], the converter output impedance is shaped to behave like a pure inductance to account for large control delays, but the stability margin may be compromised when the resistance in the grid impedance is low. Furthermore, the design of the *LC* filter is often constrained when addressing dissipativity [6, 15, 16], and this issue remains insufficiently explored.

Based on the aforementioned methods, three factors regarding passivity-based design should be considered, which are implementation easiness, dissipativity robustness, and *LC*-filter limitation. To meet these requirements at the same time, four feedforward methods are discussed including grid current feedforward, capacitor current feedforward, capacitor voltage feedforward, and the combination of capacitor current and capacitor voltage feedforward. The main findings are summarized as follows:

1) The passivity-based analytic design for capacitor current feedforward, capacitor voltage feedforward, as well as the combination of capacitor current and capacitor voltage feedforward are clarified;

2) The resonant frequency of *LC*-filters should be designed below critical frequency for grid current feedforward, while this constraint can be removed for other three feedforward methods;

3) Both grid current and capacitor current feedforward are sensitive to *LC*-filter parameter deviations, inducing a non-dissipative region around the critical frequency, while the capacitor voltage feedforward can help to enhance the dissipativity robustness;

4) The damping design is gradually simplified with an increased sampling rate. When using the double-sampling, the combination of capacitor current and capacitor voltage feedforward is mandatory for flexible *LC*-filter design and high dissipativity robustness. However, with the multi-sampling control, only proportional capacitor voltage feedforward is needed, to achieve the same performance requirement.

The remainder of the paper is structured as follows. Section II covers system modeling along with the internal stability design. In Section III, grid current feedforward is selected as the benchmark, with three key factors presented for comparison. In Section IV, the other three methods are further designed and analyzed. Section V presents the experimental results, and Section VI provides the conclusion.

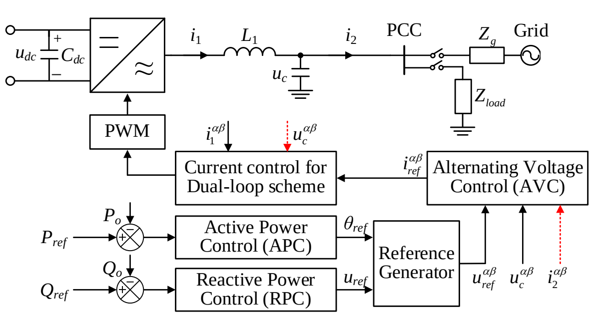

Fig. 1. The system overview of a three-phase grid-forming VSC.

II. System Modeling and Internal Stability Design

Fig. 1 shows the configuration of a three-phase grid-forming VSC. To enable alternating voltage regulation and attenuate switching harmonics, an *LC*-type filter is employed between the converter output and the point of common coupling (PCC). Active power control facilitates grid synchronization θ_{ref} while the reactive power control adjusts the amplitude of reference voltage u_{ref} . The alternating voltage control manages the capacitor voltage to track the reference voltage $u_{ref}^{\alpha\beta}$. A current control loop is cascaded with the voltage control, which aids in limiting overcurrent. [20]. In addition, the grid current i_2 , capacitor voltage u_c , and capacitor current i_c are potential feedforward variables to further enhance the stability [21]. Note that only i_2 and u_c are highlighted in red in the control diagram, this is because i_c can be acquired through the difference between i_1 and i_2 .

A. System modeling

The bandwidth of the power control loop is significantly narrower than that of the voltage control loop, which mainly affects the low-frequency stability [6, 19]. Moreover, because this paper primarily addresses the harmonic stability of voltage control, the influence of the power control loop is ignored. Besides, the model of VSC control is simplified to a single-input single-output system [9]. A passivity-based stability analysis is employed to evaluate the external stability between the VSC and the grid [8]. Specifically, the VSC is modeled as a controlled voltage source paired with an output impedance in series, as illustrated in Fig. 2. Based on that, the filter capacitor voltage is given as

$$u_c^{\alpha\beta} = \frac{1}{1+\dfrac{Z_o}{Z_g^{'}}} u_s + \frac{\dfrac{Z_o}{Z_g^{'}}}{1+\dfrac{Z_o}{Z_g^{'}}} u_g . \tag{1}$$

where u_s is the controlled voltage source, Z_o and Z_g are the converter output impedance and the grid impedance. The filter capacitance is treated as a segment of grid impedance, leading to an equivalent grid impedance given by

$$Z_g^{'} = \frac{1}{sC+\dfrac{1}{Z_g}} = \frac{Z_g}{sCZ_g+1} . \tag{2}$$

Based on the passivity theory in the frequency domain, two sufficient but not necessary conditions should be met [8]. To

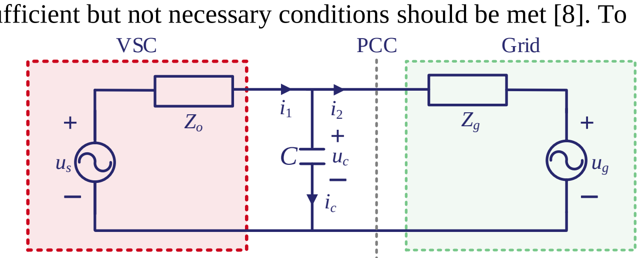

Fig. 2. Impedance model of grid-forming VSC.

ensure the internal stability, the closed-loop voltage control shall remain stable, so that the transfer function of the controlled voltage source u_s in (1) should not have right-half-plane poles. To ensure the external stability when interacting with the grid, the converter output impedance Z_o shall remain passive, whose phase angle should be designed within $[-90^\circ, 90^\circ]$. By means of that, the phase of Z_o/Z_g' can always remain $[-180^\circ, 180^\circ]$ to ensure a stable system, as the equivalent grid impedance Z_g' is already passive.

Fig. 3(a) presents the block diagram for voltage control with regular sampling. It can be found that the plant function in the feedforward path is unity when regarding the converter current i_1 as the disturbance, allowing the open-loop transfer function of the voltage control to be derived as

$$T_{ov} = G_v G_i G_d \tag{3}$$

where G_v and G_i represent the voltage controller and the current controller, respectively.

Additionally, the control delay amounts to 1.5 sampling periods [22], which can be approximated as

$$G_d \approx e^{-sT_d} = e^{-s\frac{1.5T_{sw}}{N}} \tag{4}$$

where T_{sw} is the switching period. N represents the sampling rate between the sampling frequency and the switching frequency, which is equal to one for the single-sampling PWM and two for double-sampling PWM, as illustrated in Fig. 4(a) and Fig. 4(b). Then the voltage for the controlled voltage source is given by

$$u_s = \frac{T_{ov}}{1+T_{ov}} u_{ref}^{\alpha\beta} = \frac{G_v G_i G_d}{1+G_v G_i G_d} u_{ref}^{\alpha\beta}. \tag{5}$$

Further, the converter output impedance is

$$Z_o = \frac{Z_{L1} + G_i G_d}{1 + G_v G_d}. \tag{6}$$

where $Z_{L1} = sL_1$ is the impedance of converter-side inductance.

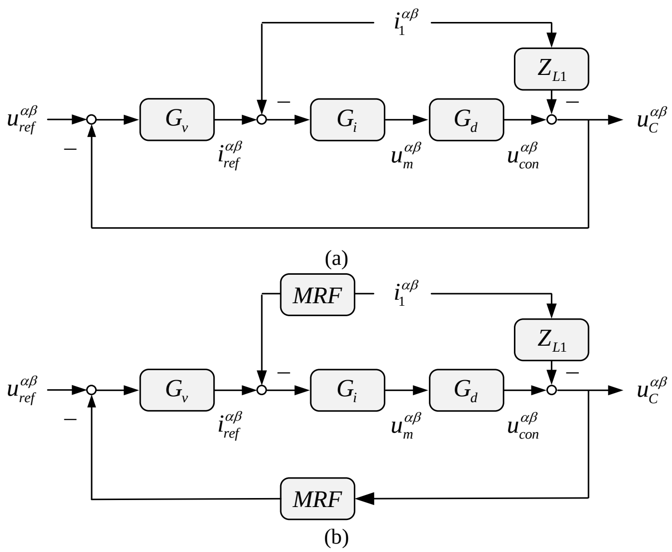

Fig. 3. Block diagram for voltage control for in three-phase grid-forming VSCs without feedforward damping. (a) With regular sampling control. (b) With multi-sampling control.

Since the control delay is the main factor affecting the harmonic instability, the multi-sampling PWM is further considered [23-24]. As shown in Fig. 4(c), for multi-sampling PWM, the sampling rate N exceeds two, and the modulation wave is updated more than twice during each switching period. Consequently, increasing the sampling rate N proportionally decreases the control delay. The control block diagram for multi-sampling voltage control in three-phase grid-forming VSCs without feedforward damping is plotted in Fig. 3(b). It can be found that the feedback path includes a modified repetitive filter (MRF), designed to eliminate multi-sampled switching harmonics and suppress the aliased low-frequency harmonics [25]. The expression of MRF is given as

$$MRF = \frac{2}{N}\frac{1-e^{-NsT_{sa}}}{1-e^{-2sT_{sa}}}\frac{1-r^N}{1-r^2}\frac{1-r^2e^{-2sT_{sa}}}{1-r^Ne^{-NsT_{sa}}} \approx e^{-\frac{sT_{sw}}{4}} \tag{7}$$

where $r \in (0, 1)$ is the attenuation factor and selected as 0.6 and 0.8 for eight-sampling and sixteen-sampling [25]. Note that the MRF can be approximated as a delay block, with the overall loop delay, including both multi-sampling PWM delay and the MRF delay, expressed as

$$T_{d,MS} = \frac{1.5T_{sw}}{N} + \frac{1}{4}T_{sw} \tag{8}$$

Based on that, the controlled voltage source and the converter output impedance for the multi-sampling control in (5) and (6) can be updated accordingly.

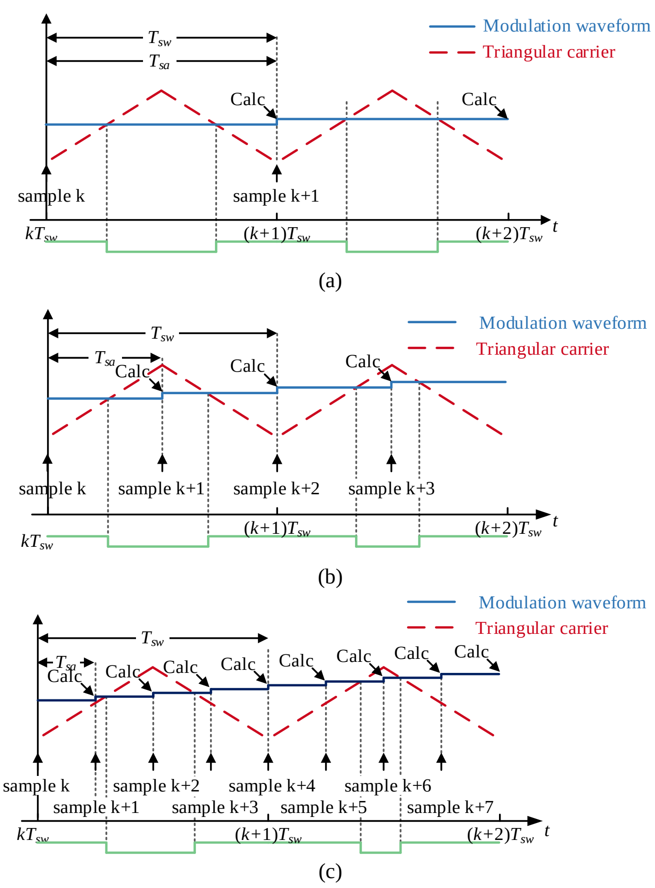

Fig. 4. Digital PWM with different sampling rates. (a) Single-sampling PWM. (b) Double-sampling PWM. (c) Multi-sampling PWM.

B. Internal stability design

Based on (3), an R controller is selected for G_v due to its advantage in simplifying the design of voltage control bandwidth. Moreover, the P part in the PR controller is equivalent to the capacitor voltage feedforward, which will be discussed in Section III. Herein, the R voltage controller is

$$G_v = K_{rv}\frac{s\cos\varphi_g - \omega_g \sin\varphi_g}{s^2 + \omega_{rc}s + \omega_g^2} \approx \frac{K_{rv}}{s} \tag{9}$$

where ω_g denotes the fundamental angle frequency, ω_{rc} represents the cut-off angle frequency, φ_g stands for the compensation angle, and K_{rv} is the gain of R controller. At high-frequencies, the behavior of the R controller closely resembles an integral controller.

On the other hand, a PR controller employed in the current control is expressed as

$$G_i = K_{pi} + K_{ri}\frac{s\cos\varphi_g - \omega_g \sin\varphi_g}{s^2 + \omega_{rc}s + \omega_g^2} \approx K_{pi} \tag{10}$$

where K_{pi} and K_{ri} represent the P gain and R gain of the current controller, respectively. Note that the R controller in (10) can be ignored in the current control loop, perticularly when analysing high-frequency stability [16]. The key approach for ensuring internal stability in a dual-loop voltage controller involves designing suitable control bandwidths for both the current and voltage control loops. The initial step is to design the current control loop, with its open-loop transfer function given as

$$T_{oi} = \frac{G_i G_d}{Z_{L1}} \approx \frac{K_{pi}e^{-sT_d}}{sL_1}. \tag{11}$$

With a defined control bandwidth ω_{ci}, the proportional gain K_{pi} is given as

$$K_{pi} = 2\pi f_{ci} L_1 = \frac{0.5\pi - \varphi_{mi}}{T_d} L_1. \tag{12}$$

where the phase margin φ_{mi} can be evaluated accordingly. Substituting (9) and (10) into (3), (3) is simplifed as

$$T_{ov} \approx \frac{K_{pi}K_{rv}e^{-sT_d}}{s}. \tag{13}$$

With a given voltage control bandwidth f_{cv}, the resonant gain K_{rv} is deduced as

$$K_{rv} = \frac{2\pi f_{cv}}{K_{pi}} = \frac{0.5\pi - \varphi_{mv}}{T_d K_{pi}}. \tag{14}$$

where the φ_{mv} is the phase margin. To decouple the voltage and the current control, f_{cv} is typically set to be lower than f_{ci}. In this paper, f_{ci} and f_{cv} is set as 1/10 and 1/20 of the sampling frequency, respectively, for double-sampling control. The same parameters are applied in the multi-sampling control. Fig. 5 shows the bode diagram for the open-loop transfer function of voltage control, with sampling rate N set at 2, 8, and 16. It is observed that multi-sampling voltage control can achive a larger phase margin compared to the double-sampling control.

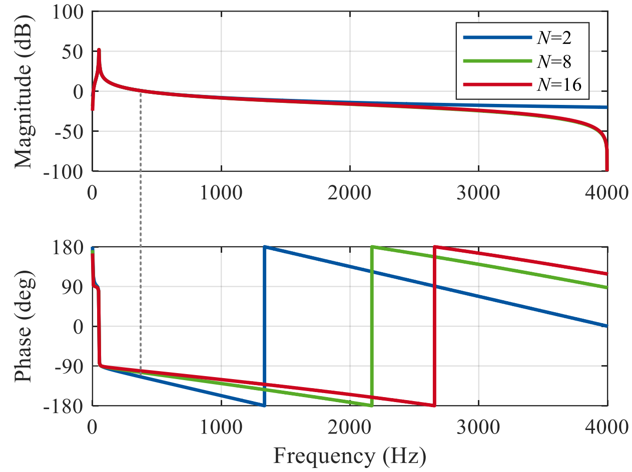

Fig. 5. Bode diagram of open-loop transfer function for the voltage control with different sampling rates.

III. Analysis for Grid Current Feedforward

To analytically solve the dissipative region of VSC, the real-part of the converter output impedance should be deduced. By replacing s with $j\omega$ in (6), the sign of $Re\{Z_o\}$ is determined as

$$\begin{aligned}\operatorname{sgn}\{\operatorname{Re}\{Z_o\}\} &= \operatorname{sgn}\{(-K_{rv}L_1 + 1)K_{pi}\cos(\omega T_d)\} \\ &= \operatorname{sgn}\{(f_{ci} - f_{cv})\cos(\omega T_d)\}.\end{aligned} \tag{15}$$

When the voltage control bandwidth f_{cv} is smaller than the current control bandwidth f_{ci}, the dissipative region without damping is given by

$$f_{dis} = (0, \frac{1}{4T_d}) = (0, f_{cr}) \tag{16}$$

where f_{cr} is defined as the critical frequency. The converter output impedance without damping is presented in Fig. 6, and it is observed that the phase of output impedance falls within the range of $[-90^\circ, 90^\circ]$ when the frequency exceeds the critical frequency threshold. Moreover, the dissipative region is extended with multi-sampling due to its reduced delay and increased critical frequency.

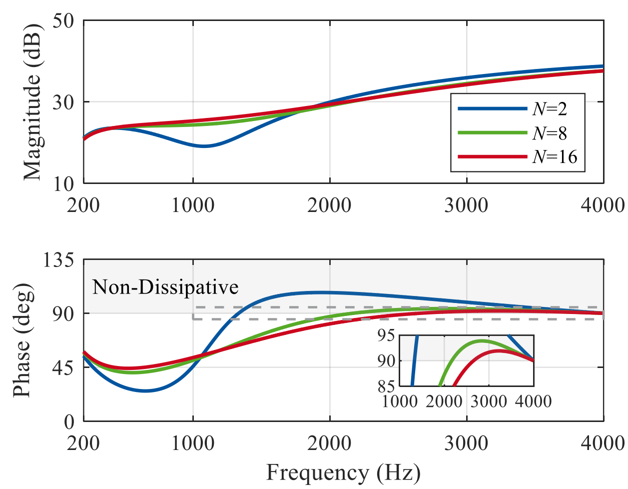

Fig. 6. Converter output impedance without damping.

However, additional damping is necessary to further optimize the dissipative bound to switching frequency, which is 4 kHz in this paper. Proportional grid current feedforward is frequency discussed in the previous research, which has been proved an effective solution to improve the dissipativity [9]. As shown in Fig. 7, the grid current feedforward (red block) is depicted alongside the derivative capacitor voltage feedforward and the converter current feedforward, which can be explained through (17).

$$G_f^{i_2} i_2^{\alpha\beta} = G_f^{i_2}(i_1^{\alpha\beta} - i_c^{\alpha\beta}) = G_f^{i_2}(i_1^{\alpha\beta} - sCu_c^{\alpha\beta}) \tag{17}$$

where $G_f^{i_2}$ is the coefficient of grid current feedforward. Based on that, the output impedance Z_o is given as

$$Z_o = \frac{sL_1 + G_i G_d (1 + G_f^{i_2})}{1 + G_i G_d (G_v - sCG_f^{i_2})}. \tag{18}$$

By replacing s with $j\omega$ in (18), the sign of $Re\{Z_o\}$ is

$$\operatorname{sgn}\{\operatorname{Re}\{Z_o\}\} = \operatorname{sgn}\{(-K_{rv}L_1 + 1 + G_f^{i_2}(1 - L_1C\omega^2))K_{pi}\cos(\omega T_d)\}. \tag{19}$$

As the sign of (19) is determined by 'cos(ωT_d)', $G_f^{i_2}$ can be deduced by letting (19) equal to zero at the critical frequency:

$$G_f^{i_2} = \frac{K_{rv}L_1 - 1}{1 - \dfrac{f_{cr}^2}{f_{LC}^2}} \tag{20}$$

where f_{LC} is the LC-filter resonance frequency. As shown in Fig. 8, the phase of converter output impedance falls between -90° to 90°, indicating the dissipation is achieved below the switching frequency for both regular- and multi-sampling controls.

However, $G_f^{i_2}$ is dependent on the LC-filter parameters, which will affect the robustness. Fig. 9 shows that the converter output impedance with ±20% parameter deviation of LC-filter, revealing a non-dissipative region near the critical frequency. Note that the multi-sampling control does not show a significant advantage compared with double-sampling control regarding robustness.

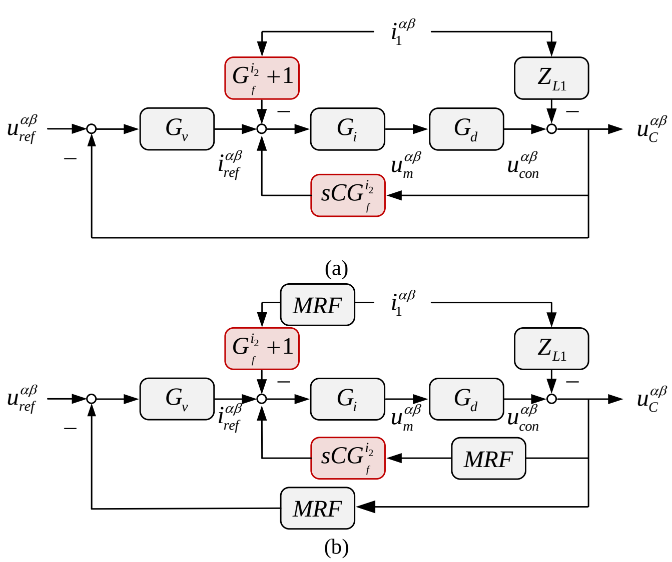

Fig. 7. Block diagram for voltage control in three-phase grid-forming VSCs with grid current feedforward damping. (a) With regular sampling control. (b) With multi-sampling control.

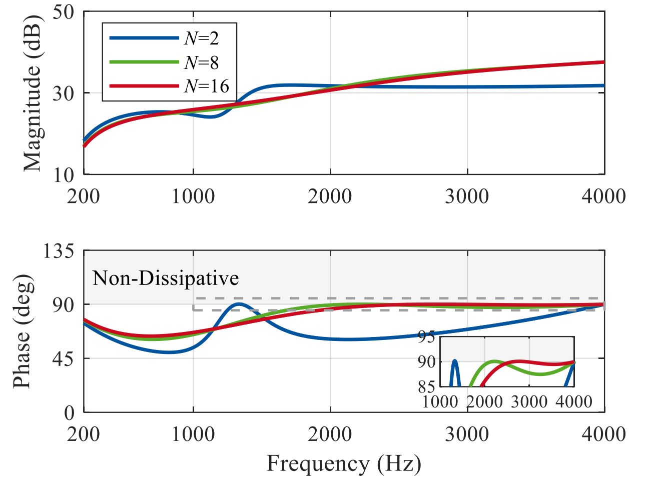

Fig. 8. Converter output impedance with grid current feedforward damping and the f_{LC} is low.

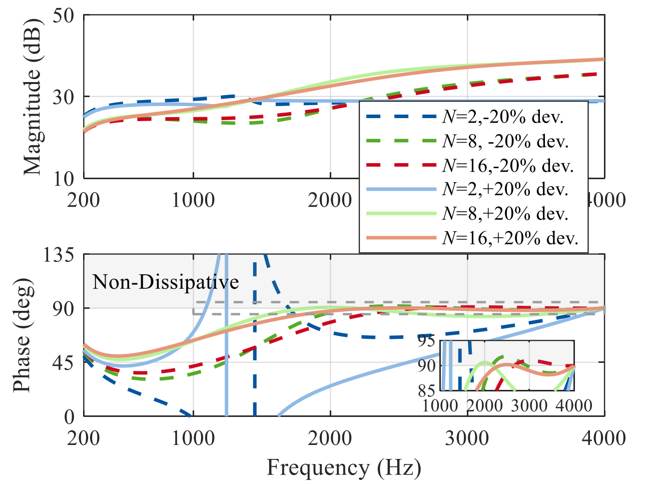

Fig. 9 The effect of parameter deviation on the converter output impedance with grid current feedforward damping when f_{LC} is low.

Besides, the f_{LC} should be set below f_{cr}, otherwise the grid current feedforward damping method will lose effectiveness, as shown in Fig. 10. Recalling (20), (19) can be rewritten as

$$\operatorname{sgn}\{\operatorname{Re}\{Z_o\}\} = \operatorname{sgn}\left\{\frac{f_{cr}^2 - f^2}{f_{cr}^2 - f_{LC}^2}\cos(\omega T_d)\right\}. \tag{21}$$

It can be found that (21) remains negative when f_{LC}> f_{cr} under double-sampling control, and the phase of converter output impedance falls outside the range $[-90^\circ, 90^\circ]$. Moreover, multi-sampling grid current feedforward damping can still maintain the dissipativity. This is due to f_{LC} typically being set below half of the switching frequency to filter the switching harmonics, while f_{cr} for multi-sampling control exceeds half the switching frequency, as indicated in(8) and (16). On the other hand, based on (4), the f_{cr} is only 1/6 and 1/3 of the switching frequency for single- and double-sampling control.

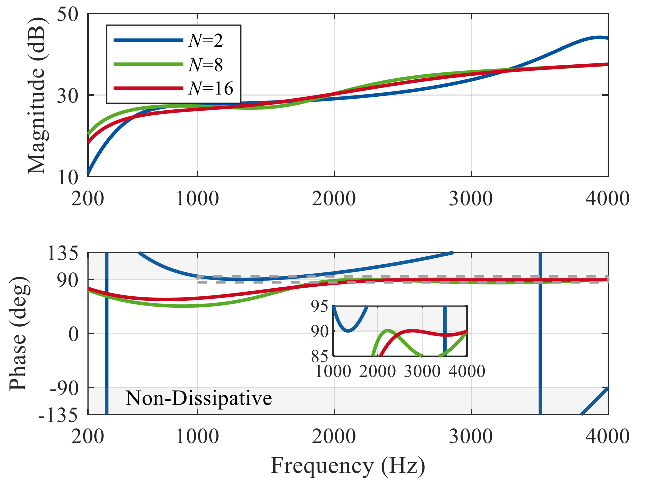

Fig. 10. Converter output impedance with grid current feedforward damping when f_{LC} is high.

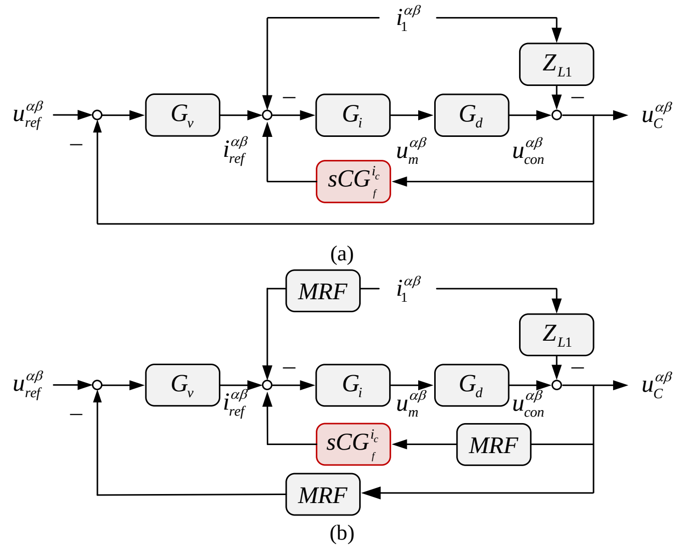

Fig. 11. Block diagram for voltage control in three-phase grid-forming VSCs with capacitor current feedforward damping.

IV. External Stability Enhancement

To achieve greater flexibility in designing the LC filter resonance frequency and improve robustness against parameter deviations, various feedforward control schemes are explored. A range of feedforward control schemes are explored utilizing both regular- and multi-sampling techniques, and the feedforward variables can be capacitor current, capacitor voltage, and a combined approach of both.

A. Capacitor current feedforward

According to Fig. 7, the effect of using grid current feedforward is the same as using the feedforward of converter current and capacitor current, provided that the feedforward coefficients are identical. Further, reanalyzing the term '$G_f^{i_2}(1-L_1C\omega^2)$' in (19), the capacitor current feedforward is the main factor in shaping the converter output impedance, and the converter current feedforward can only change the amplitude of (19) instead of the sign. Hence, only capacitor current feedforward is used for active damping, as shown in Fig.11. Then the VSC output impedance is

$$Z_o = \frac{sL_1 + G_i G_d}{1 + G_i G_d G_v - sCG_i G_f^{i_c} G_d} \tag{22}$$

where $G_f^{i_c}$ is the capacitor current feedforward coefficient. Note that the converter output impedance depends on both feedforward function and feedback control parameters. By replacing s with $j\omega$ in (22), the sign of $Re\{Z_o\}$ is

$$\operatorname{sgn}\{\operatorname{Re}\{Z_o\}\} = \operatorname{sgn}\{(-K_{rv}L_1 + 1 - G_f^{i_c} L_1 C\omega^2)K_{pi}\cos(\omega T_d)\}. \tag{23}$$

By letting (23) be zero at the critical frequency f_{cr}, $G_f^{i_c}$ is

$$G_f^{i_c} = \frac{1-K_{rv}L_1}{\dfrac{f_{cr}^2}{f_{LC}^2}}. \tag{24}$$

Compared with (20), it can be found that $G_f^{i_c}$ will always be a limited value especially when $f_{LC} = f_{cr}$, which means that the LC-filter design limitation is removed. Moreover, with the capacitor current feedforward, multi-sampling conrol does not offer significant advantanges over double-sampling control when considering the design flexibility of the f_{LC}. To further validate this finding, (24) is substituted into (23), which is rewritten as

$$\operatorname{sgn}\{\operatorname{Re}\{Z_o\}\} = \operatorname{sgn}\{(f_{cr}^2 - f^2)\cos(\omega T_d)\}. \tag{25}$$

The same conclusion can be obtained by comparing (21) and (25). As shown in Fig. 12, the dissipativity can still be achieved even though the f_{LC} is higher than f_{cr} with double-sampling control. However, the robustness of dissipativity near the critical frequency is weak when there is a ±20% deviation in *LC*-filter parameters, as depicted in Fig. 13. This is because $G_f^{i_c}$ is related to the practical *LC*-filter parameters.

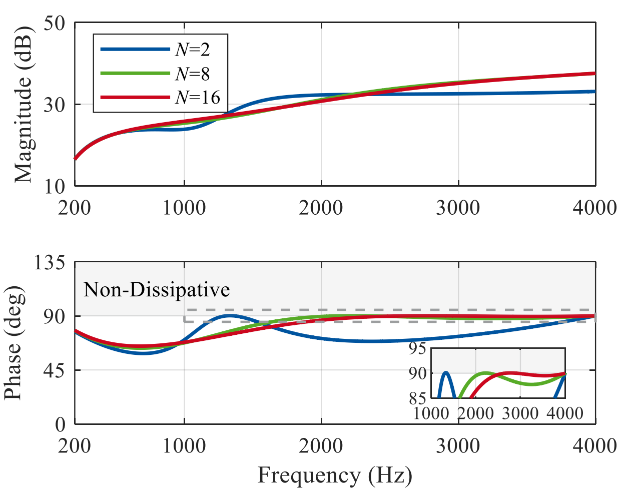

Fig. 12. Converter output impedance with capacitor current feedforward damping when f_{LC} is high.

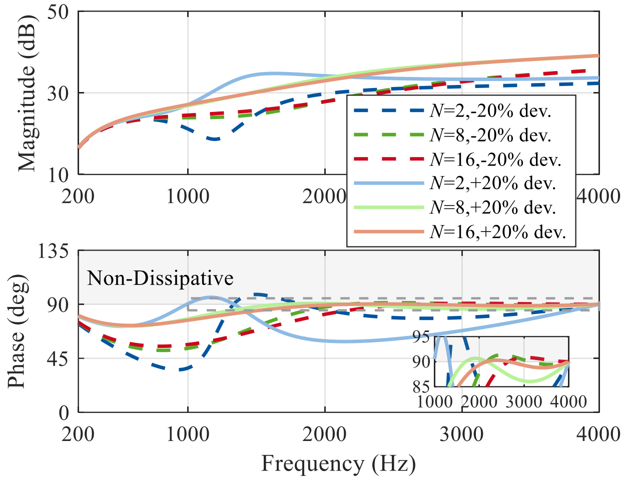

Fig. 13. The effect of parameter deviation on the converter output impedance with capacitor current feedforward damping when f_{LC} is high.

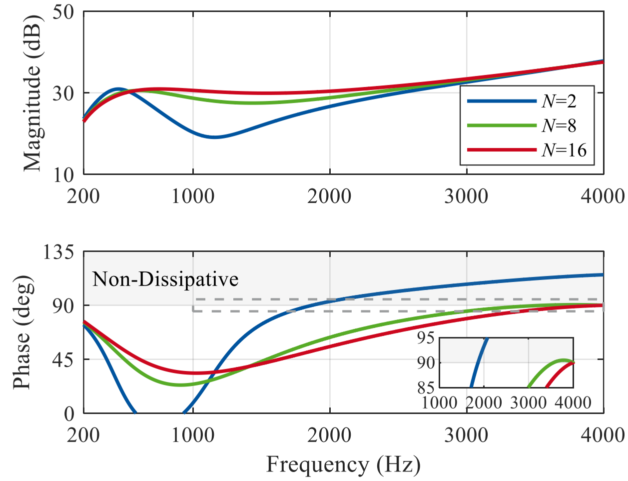

Fig. 15. Converter output impedance with capacitor voltage feedforward damping when f_{LC} is high.

B. *Capacitor voltage feedforward*

Capacitor voltage feedforward is frequently employed in grid-following VSCs to enhance dynamics and stability [26], so it is necessary to investigate its effect on the voltage control of grid-forming VSCs, as illustrated in Fig. 14. The output impedance of the VSC with proportional capacitor voltage feedforward is

$$Z_o = \frac{sL_1 + G_i G_d}{1 + G_i G_d G_v - G_f^{u_c} G_d} \tag{26}$$

where $G_f^{u_c} = K_f^{u_c}$ is the feedforward coefficient. By replacing s with $j\omega$ in (26), the sign of $Re\{Z_o\}$ is determined as

$$\operatorname{sgn}\{\operatorname{Re}\{Z_o\}\} = \operatorname{sgn}\left\{\begin{matrix}(-K_{rv}L_1+1)K_{pi}\cos(\omega T_d) \\ +(L_1\sin(\omega T_d)\omega - K_{pi})K_f^{u_c}\end{matrix}\right\}. \tag{27}$$

It should be noted that an extra term '$L_1\sin(\omega T_d)\omega$' is introduced, which can notably widen the dissipative region. As demonstrated in Fig. 15, dissipativity below the switching frequency is achieved when the sampling rate is sufficiently high, such as N=16, due to the lower control delay. This means

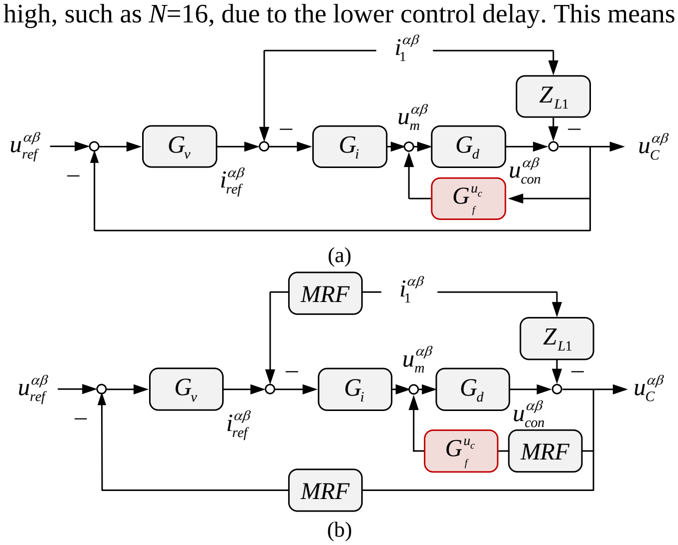

Fig. 14. Block diagram for voltage control in three-phase grid-forming VSCs with capacitor voltage feedforward damping.

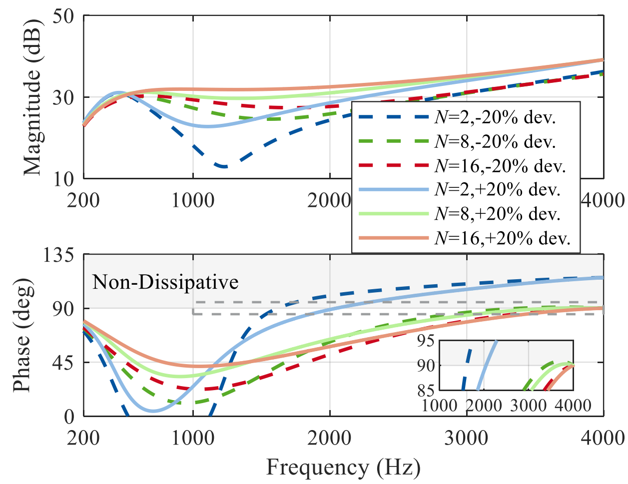

Fig. 16. The effect of parameter deviation on the converter output impedance with capacitor voltage feedforward damping when f_{LC} is high.

that only the voltage sensors and the converter current sensors are needed for the damping when using multi-sampling control, which is more suitable for commercial applications. On the other hand, the sixteen-sampling control has a high robustness against parameter deviation of LC-filters, as presented in Fig. 16.

C. *Capacitor voltage and capacitor current feedforward*

Based on the previous analysis, it is evident that the capacitor current feedforward can effectively eliminate most of the non-dissipative regions, while capacitor voltage feedforward improves the dissipativity robustness near the critical frequency. Hence, it is necessary to investigate the combination of two feedforward methods especially for the double-sampling control and eight-sampling control. Based on Fig. 17, the converter output impedance is given as

$$Z_o = \frac{sL_1 + G_i G_d}{1 + G_i G_d G_v - sCG_i G_f^{i_c} G_d - G_f^{u_c} G_d}. \tag{28}$$

When the feedforward coefficients $G_f^{i_c}$ and $G_f^{u_c}$ are constants, the sign of $Re\{Z_o\}$ is given as

$$\operatorname{sgn}\left\{\operatorname{Re}\left\{Z_o\right\}\right\}=\operatorname{sgn}\left\{\begin{array}{l}(-K_{rv}L_1+1-G_f^{i_c}L_1C\omega^2)K_{pi}\cos(\omega T_d)\\+(L_1\sin(\omega T_d)\omega-K_{pi})K_f^{u_c}\end{array}\right\}. \tag{29}$$

Especially, the Re{Z_o} at the switching frequency for double-sampling control is a large negative number because the term '$\sin(0.5\omega_{sa}1.5T_{sa})$' in (29) is -1, and the first step is to modify the capacitor voltage feedforward function. Specifically, an additional delay of $0.5T_{sa}$ can be introduced into the capacitor voltage feedforward path, causing the term '$\sin(0.5\omega_{sa}2T_{sa})$' in (29) to become zero. In real-world application, a moving average filter is selected, which is

$$G_f^{u_c}=K_f^{u_c}(0.5+0.5e^{-sT_{sa}}). \tag{30}$$

As depicted in Fig. 18, the improved capacitor voltage feedforward successfully achieves dissipation for double-sampling. Additionally, the dissipation is also achieved for

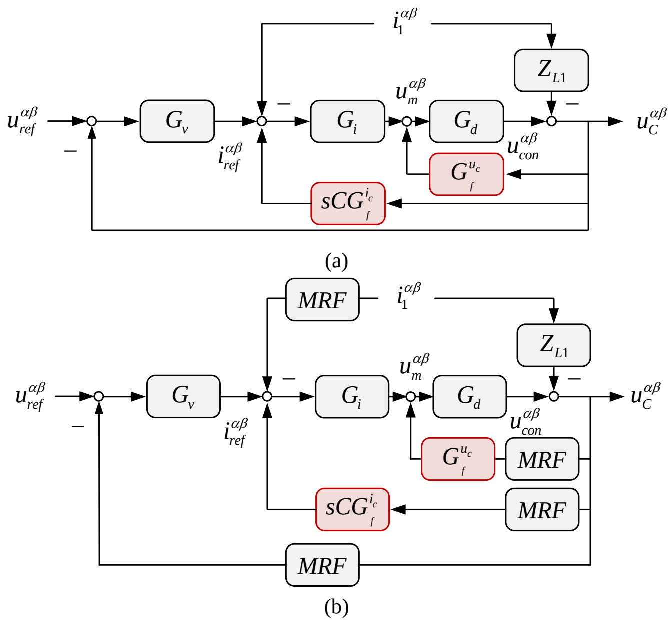

Fig. 17. Block diagram for voltage control in three-phase grid-forming VSCs with capacitor voltage feedforward damping and capacitor current feedforward damping.

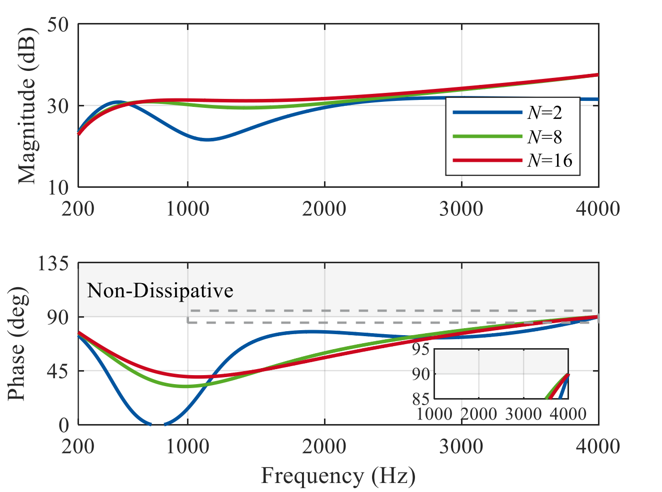

Fig. 18. Converter output impedance with modified capacitor voltage feedforward damping and capacitor current feedforward damping when f_{LC} is high.

eight-sampling control when using proportional capacitor voltage feedforward and proportional capacitor current feedforward. Further, it is understandable that the dissipation can be achieved for sixteen-sampling due to its low delay. However, -20% parameter deviation of LC-filter can still threaten the dissipativity for the double-sampling control, as seen in Fig. 19. Therefore, the capacitor current feedforward coefficient $G_f^{i_c}$ is modified by inserting a correction factor x to offset the effect of negative parameter deviation, which is

$$G_f^{i_c}=\frac{1-K_{rv}L_1x}{L_1Cx^2\omega_{cr}^2}. \tag{31}$$

where x is set as 0.8. Moreover, to further enhance the dissipativity, (31) can be used for the multi-sampling control. It can be found from Fig. 20 that the double-sampling control demonstrates high robustness comparable to that of multi-sampling control. Unlike the case with grid current feedforward, introducing the capacitor voltage feedforward and the capacitor current feedforward results in the coupling of open-loop internal stability with the dissipative characteristic.

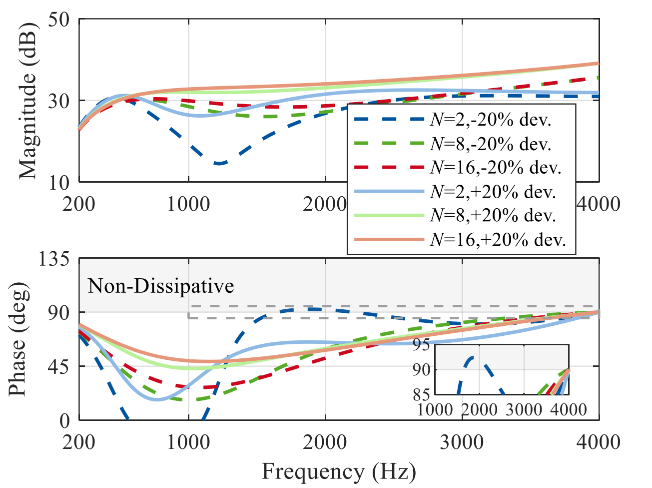

Fig. 19. The effect of parameter deviation on the converter output impedance with modified capacitor voltage feedforward damping and capacitor current feedforward damping when f_{LC} is high.

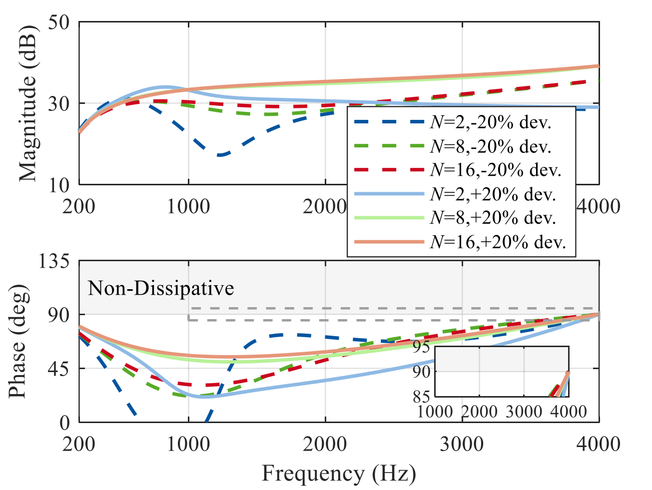

Fig. 20. The effect of parameter deviation on the converter output impedance with modified capacitor voltage feedforward damping and modified capacitor current feedforward damping when f_{LC} is high.

TABLE I
COMPARISON AMONG DIFFERENT FEEDFORWARD DAMPING METHOD

Type		Feedforward Function	Voltage Feedback Controller Parameter	Implementation	Dissipation	Dissipativity Robustness	*LC*-Filter Design Constraint for Dissipation
Method I: Grid Current Feedforward [6, 9]	*N*=2	$G_f^{i_2}=\frac{K_{rv}L_1-1}{1-\frac{f_{cr}^2}{f_{LC}^2}}$	$K_{rv}=\frac{2\pi f_{cv}}{K_{pi}}$	Extra Grid Current Sensor	√	Weak	$(0,f_{cr})\Rightarrow(0,\frac{1}{3}f_{sw})$
	N=8						$(0,f_{cr})\Rightarrow(0,\frac{4}{7}f_{sw})$
	N=16						$(0,f_{cr})\Rightarrow(0,\frac{8}{11}f_{sw})$
Method II: Capacitor Current Feedforward	*N*=2	$G_f^{i_c}=\frac{1-K_{rv}L_1}{\frac{f_{cr}^2}{f_{LC}^2}}$	$K_{rv}=\frac{2\pi f_{cv}}{K_{pi}}$	Extra Grid/Capacitor Current Sensor	√	Weak	$(0,f_{sw})$
	N=8						
	N=16						
Method III: Capacitor Voltage Feedforward	*N*=2	$G_f^{u_c}=K_f^{u_c}$	$K_{rv}=\frac{2\pi f_{cv}(1-K_f^{u_c})}{K_{pi}}$	Simple	×	Weak	$\approx(0,\frac{2}{3}f_{sw})$
	N=8			Simple	×	Strong	$\approx(0,f_{sw})$
	N=16			Simple	√	Strong	$(0,f_{sw})$
Method IV: Capacitor Voltage and Current Feedforward	*N*=2	$G_f^{u_c}=K_f^{u_c}(0.5+0.5e^{-sT_{sa}})$ $G_f^{i_c}=\frac{1-K_{rv}L_1x}{L_1Cx^2\omega_{cr}^2}$	$K_{rv}=\frac{2\pi f_{cv}(1-K_f^{u_c})}{K_{pi}}$	Extra Grid/Capacitor Current Sensor	√	Strong	$(0,f_{sw})$
	N=8	$G_f^{u_c}=K_f^{u_c}$ $G_f^{i_c}=\frac{1-K_{rv}L_1x}{L_1Cx^2\omega_{cr}^2}$					
	N=16						

Remark: f_{cr}: critical frequency; f_{LC}: *LC*-filter resonance frequency; f_{sw}: switching frequency; blue part: recommended feedforward damping method.

Recalling Fig. 17, the transfer function related to the internal stability is

$$T_{ov}=\frac{G_vG_iG_d}{1-G_f^{u_c}G_d-sCG_iG_f^{i_c}G_d}\approx\frac{K_{rv}K_{pi}e^{-sT_d}}{s(1-K_f^{u_c})} \tag{32}$$

where the effect of capacitor current feedforward on the internal stability can be ignored due to its low amplitude. Then the coefficient for the voltage controller is

$$K_{rv}=\frac{2\pi f_{cv}(1-K_f^{u_c})}{K_{pi}}. \tag{33}$$

Moreover, $K_f^{u_c}$ is recommended to be designed below 1 to make K_{rv} larger than 0, and the similar finding can be found in [27]. When $K_f^{u_c}$ increases from 0.5 to 0.9, as shown in Fig. 21, the phase margin of (32) is reduced. Additionally, the practical bandwidth cannot follow the target value, which makes (33) non-accurate. Regarding the controller design simpleness and the enough phase margin, $K_f^{u_c}$ is set as 0.5 in this paper.

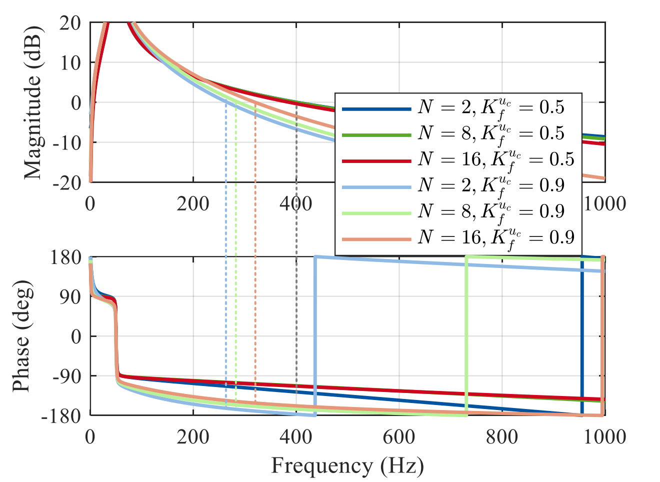

Fig. 21. Effect of capacitor voltage feedforward coefficients on the open-loop transfer function for the voltage control.

D. Comparison

To further illustrate the similarities and the differences among the previous discussed feedforward damping methods, six aspects regarding the feedforward function, voltage controller parameter, implementation, dissipation, dissipativity robustness, and *LC*-filter design constraint for dissipation, are summarized in Table I. Note that both feedforward functions and feedback control parameters shall be carefully designed to ensure dissipation and dissipativity robustness against filter parameter deviations.

First, the capacitor voltage sensor and converter current sensor are essential for basic voltage and current control functions. However, methods I, II, and IV require additional current sensors, which increase the overall cost. It is worth noticing that in method II, the capacitor current can be sampled directly or determined by the difference between the sampled converter current and the sampled grid current. Method III, on the other hand, offers the simplest implementation, relying solely on capacitor voltage feedforward without the need for extra sensors.

Second, while methods I and II achieve dissipation below the switching frequency, they exhibit weak robustness in dissipativity when faced with parameter deviations. This weakness arises due to the phase of the converter output impedance being 90° at the critical frequency. However, introducing capacitor voltage feedforward, as implemented in method IV, greatly enhances the dissipativity and improves the dissipation performance. Additionally, the performance of method III improves progressively with an increase in the sampling rate, both in terms of dissipativity robustness and dissipation. Notably, method III with sixteen-sampling, the preferred approach, can achieve a performance comparable to that of method IV.

Third, regarding method I, the f_{LC} must be below f_{cr} required for dissipation; typically, it is also designed to be less than half of the switching frequency for suppressing switching ripple. In a double-sampling control system, this design approach will introduce a forbidden region for the *LC* filter, necessitating that the resonance frequency must falls be lower than the critical frequency. However, this constraint is not applicable to a multi-sampling control system, where the critical frequency often exceeds half of the switching frequency. On the other hand, it can be found that the constraint for the *LC*-filter design can be removed when the dissipation is achieved, as seen in method II and method IV. Although method III with double-sampling still has a constraint, the *LC*-filter resonance frequency is usually not designed to exceed two-thirds of the switching frequency. Furthermore, method III with multi-sampling can remove this design constraint.

V. Experimental Validation

To further validate the proposed method, experiments were conducted on a three-phase grid-forming converter from Imperix, as depicted in Fig. 22, with the system parameters listed in Table II. The linear amplifier APS 15000 is used to emulate the grid. As discussed in Section III.E, method III with sixteen-sampling not only achieves effective dissipation but also offers strong robustness and simple implementation. Therefore, this method is recommended in this paper and validated through experiments. For comparison, the conventional grid current feedforward method with double-sampling control is also tested.

The first set of experiments are carried out to validate the main disadvantage for method I with double-sampling, i.e., the f_{LC} must be below the critical frequency for effective dissipation. Herein, the critical frequency for double-sampling control is $f_{cr} = \dfrac{8000}{6} \approx 1333$ Hz, and the f_{LC} is set as 1678 Hz where L_1=3 mH and C=3 μF. A CL filter is used to emulate the grid impedance Z_g where L_g=3 mH and C_g=10 mH. As shown in Fig. 23, since f_{LC} is larger than f_{cr} for double-sampling control, the phase of Z_o for method I is always out of $[-90^\circ, 90^\circ]$, which makes the phase difference with $Z_g^{'}$ beyond 180° at the intersection point. According to the Nyquist stability criterion, this condition will render the system unstable.

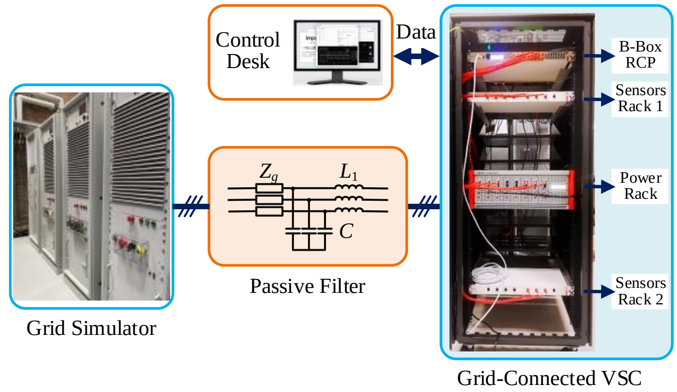

Fig. 22. A down-scale three-phase LC-filtered converter.

TABLE II
System Parameters

Symbol	Description	Value
S_n	Apparent power	3.5 kVA
u_g	Line RMS voltage	190 V
L_1	Converter inductance	3 mH
C	Filter capacitance	3/10 μF
f_{sw}	Switching frequency	4 kHz
f_{sa}	Sampling frequency	8/64 kHz

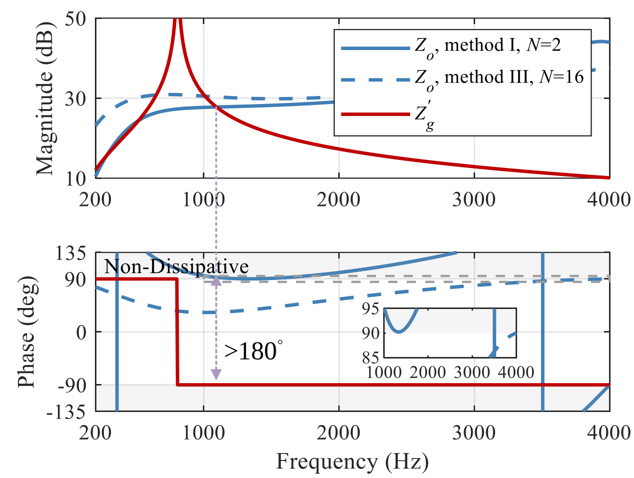

Fig. 23. Bode diagram of converter output impedance and grid impedence with grid current feedforward (N=2) and capacitor voltage feedforward (N=16), and f_{LC} is higher than f_{cr} with double-sampling control.

On the other hand, regarding method III with sixteen-sampling, the reduced delay combined with the capacitor voltage feedforward makes the converter output impedance to be dissipative below the swiching frequency (4000 Hz) thus ensuring the stability with the grid. The corresponding experimentalresults , capturing the capcitor voltage, the converter current, and the grid current are shown in Fig. 24. Due to the wide non-dissipative region, the method I with double-sampling is triped immediately at the starting instant (see Fig. 24(a)). When adopting the method III with sixteen-sampling

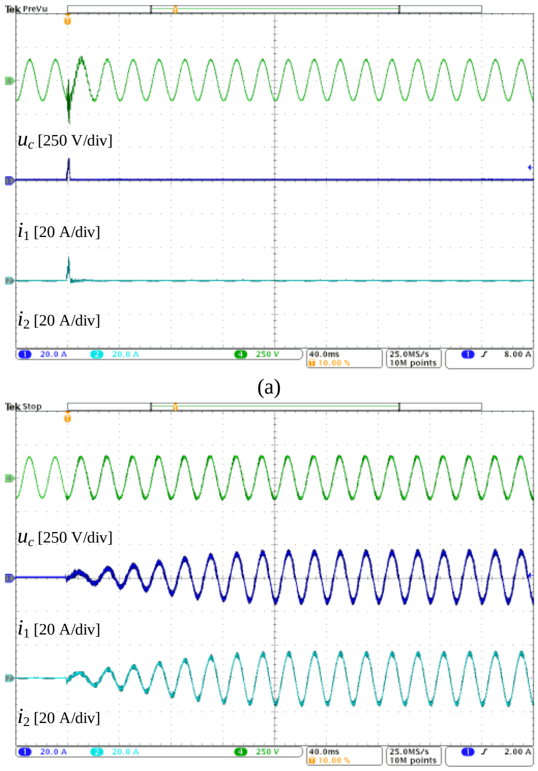

(a)

(b)

Fig. 24. Experimental results of dual-loop voltage control when f_{LC} is higher than f_{cr} with double-sampling control. (a) Grid current feedforward damping with double-sampling. (b) Capacitor voltage feedforward damping with sixteen-sampling.

(see Fig. 24(b)), the system becomes stable thus verifying the theoretical analysis in Fig. 23.

The second set of experiments are conducted to evaluate the robustness against the parameter deviation in the LC-filter. For method I with double-sampling control, the nominal f_{LC} must be below the critical frequency to ensure the dissipation in the absence of parameter deviation. Herein, the f_{LC} is set as 919 Hz with L_1=3 mH and C=10 μF. A CL filter is used to emulate the grid impedance Z_g where L_g=3 mH and C_g=10 mH. As shown in Fig. 25, for method I with double-sampling, there is a non-dissiaptive region around the critical frequency (1333 Hz) with a -20% deviation of LC- filter parameters. The weak robustness results in the phase difference between Z_o and $Z_g^{'}$ exceeding 180° thus disstablizing the system.

The related experimental validation is illustrated in Fig. 26. With the method I using the conventional double-sampling, high-frequency resonance is observed in Fig. 26(a) due to the non-dissipative region induced by the PWM delay. Compared to Fig. 24(a), the VSC is not triped instantly because of the narrow non-dissipative region. Using method III with sixteen-sampling significantly boosts the dissipativity robustness, as presented in Fig. 25. Specifically, the phase of converter output impedance at the critial frequency is far away from the boundary 90° and -90°. The experimental result in Fig. 26(b) demonstrates the effectiveness of the method III with sixteen-sampling control.

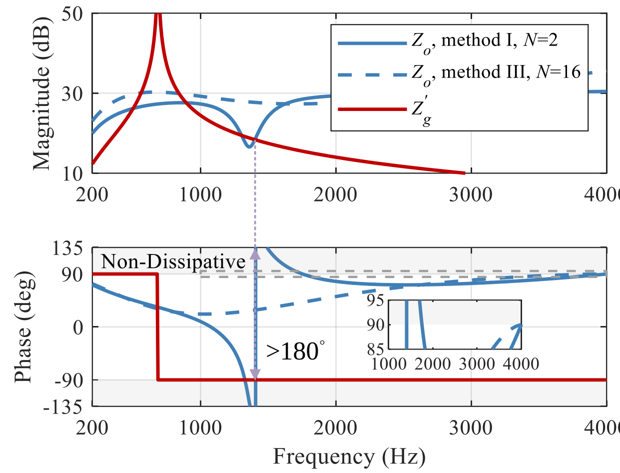

Fig. 25. Bode diagram of converter output impedance and grid impedence with grid current feedforward (N=2) and capacitor voltage feedforward (N=16), and f_{LC} is lower than f_{cr} with double-sampling control. but with -20% parameter deviation.

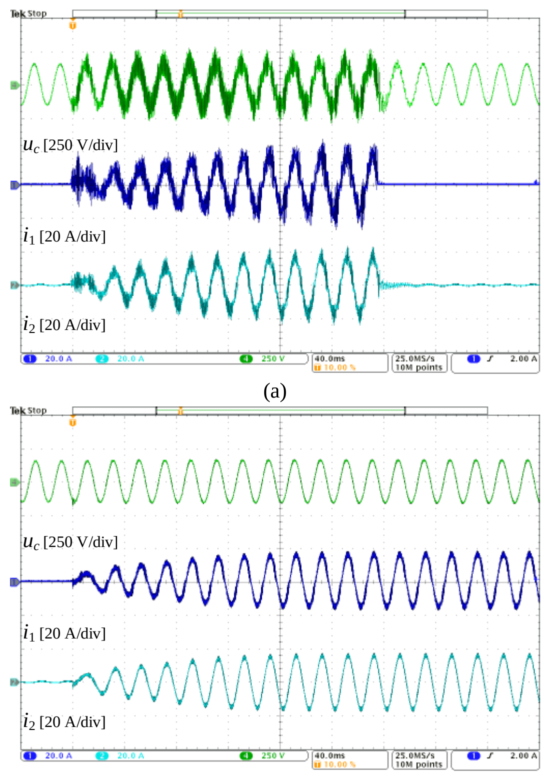

(a)

(b)

Fig. 26. Experimental results of voltage control considering a -20% parameter deviation of LC-filter and f_{LC} is lower than f_{cr} with double-sampling control. (a) Grid current feedforward damping with double-sampling. (b) Capacitor voltage feedforward damping with sixteen-sampling.

The third set of experiments are implemented to test the transient performance under a strong grid, where the active power reference steps from 0.5 p.u. to 1 p.u at 96 ms (see Fig. 27). Moreover, the grid inductance L_g is set as 1 mH, indicating a short-circuit ratio of 33. To make sure that the method I with double-sampling is also stable, the resonance frequency of the LC-filter is set as 919 Hz (< f_{cr} = 1333 Hz) for both control methods. It can be found that the proposed method III with sixteen-sampling has similar performance to method I with double-sampling. This is because the dynamics of the power loop is much slower than voltage and current control loops.

The fourth set of experiments are implemented to test the transient performance under island operations, where the reference voltage steps from 0.5 p.u. to 1 p.u at 120 ms (see Fig. 28). In this case, an *RL* load is selected where R_{load} = 57 Ω and L_{load} = 1 mH. Similar to the third set of experiments, the *LC*-filter resonance frequency is set as 919 Hz (< f_{cr} = 1333 Hz) for both control methods. Note that the proposed method III with sixteen-sampling has similar performance to the method I with double-sampling.

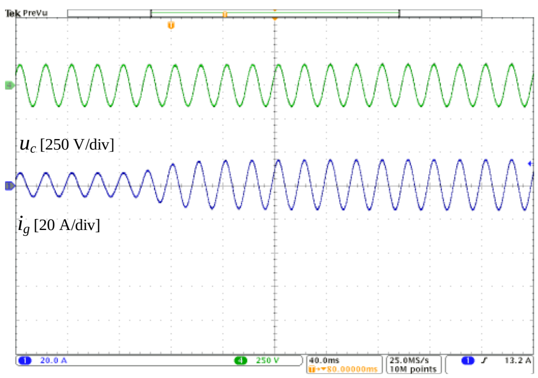

(a)

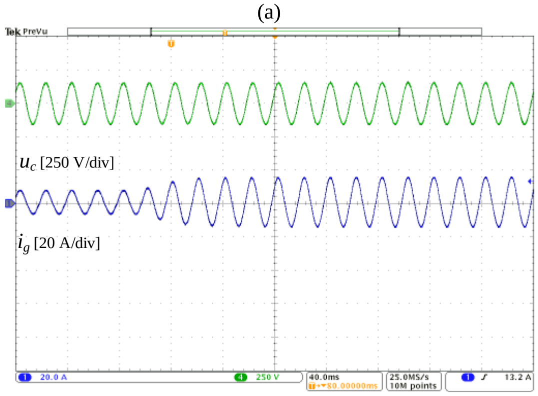

(b)

Fig. 27. Experimental results of a power transient (f_{LC} is lower than f_{cr} with double-sampling control). (a) Grid current feedforward damping with double-sampling. (b) Capacitor voltage feedforward damping with sixteen-sampling.

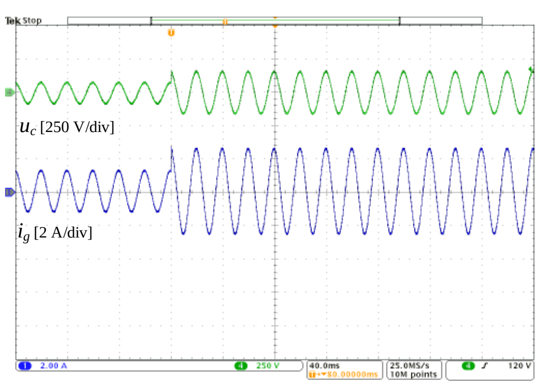

(a)

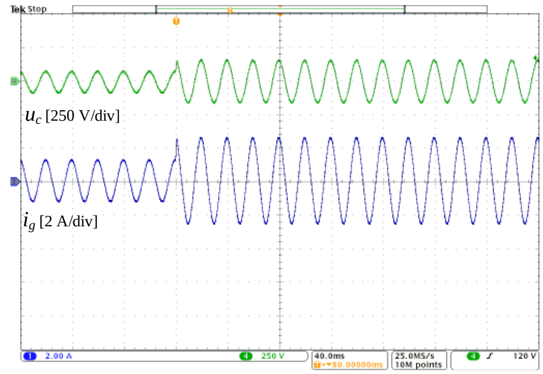

(b)

Fig. 28. Experimental results of a voltage transient (f_{LC} is lower than f_{cr} with double-sampling control). (a) Grid current feedforward damping with double-sampling. (b) Capacitor voltage feedforward damping with sixteen-sampling.

VI. Conclusion

This paper examines the impact of control delay and sampling rates on voltage control schemes for grid-forming VSCs from a passivity perspective. Three key limitations have been identified in the commonly used grid current feedforward damping method: 1) *LC*-filter design constraints, 2) weak dissipativity robustness against LC-filter parameter deviations, and 3) the requirement for additional current sensors. It is observed that combining capacitor current and capacitor voltage feedforward can overcome the first two limitations. Furthermore, sixteen-sampling capacitor voltage feedforward is recommended, as it can effectively resolve all three limitations and has similar dynamics to the grid current feedforward damping method. The effectiveness of the proposed method is demonstrated through experiments.

References

[1] L. Orellana, L. Sainz, E. Prieto-Araujo, and O. Gomis-Bellmunt, "Stability assessment for multi-infeed grid-connected VSCs modeled in the admittance matrix form," *IEEE Trans. Circuits Syst. I, Reg. Papers*, vol. 68, no. 9, pp. 3758–3771, Sep. 2021.

[2] Z. Wang, P. Cheng, H. Pan, and L. Jia, "Impedance-circuit-based stability analysis for PLL-synchronized voltage source converter in weak grid," *IEEE Trans. Circuits Syst. I, Reg. Papers, early access*, Nov. 2023.

[3] D. B. Rathnayake *et al*., "Grid forming inverter modeling, control, and applications," *IEEE Access*, vol. 9, pp. 114781-114807, 2021.

[4] Y. Li, T. C. Green, and Y. Gu, "The intrinsic communication in power systems: A new perspective to understand synchronization stability," *IEEE Trans. Circuits Syst. I, Reg. Papers*, vol. 70, no. 11, pp. 4615–4626, Nov. 2023.

[5] M. J. Li and C. K. Tse, "Where should inverter-based resources be located in power networks?" *IEEE Trans. Circuits Syst. I, Reg. Papers*, vol. 71, no. 3, pp. 1456–1464, Mar. 2024.

[6] G. Wu, Y. He, H. Zhang, X. Wang, D. Pan, X. Ruan, and C. Yao, "Passivity-based stability analysis and generic controller design for grid-forming inverter," *IEEE Trans. Power Electron*., vol. 38, no. 5, pp. 5832-5843, May 2023.

[7] X. Wang, M. G. Taul, H. Wu, Y. Liao, F. Blaabjerg, and L. Harnefors, "Grid-synchronization stability of converter-based resources–an overview," *IEEE Open J. Ind. Appl*., vol. 1, pp. 115–134, Aug. 2020.

[8] L. Harnefors, A. G. Yepes, A. Vidal, and J. Doval-Gandoy, "Passivity-based controller design of grid-connected VSCs for prevention of electrical resonance instability," *IEEE Trans. Ind. Electron*., vol. 62, no. 2, pp. 702–710, Feb. 2015.

[9] Y. Liao, X. Wang, and F. Blaabjerg, "Passivity-based analysis and design of linear voltage controllers for voltage-source converters," *IEEE Open J. Ind. Electron. Soc*., vol. 1, pp. 114–126, June 2020.

[10] X. Wang, P. C. Loh, and F. Blaabjerg, "Stability analysis and controller synthesis for single-loop voltage-controlled VSIs," *IEEE Trans. Power Electron.*, vol. 32, no. 9, pp. 7394–7404, Sep. 2017.

[11] X. Li, P. Lin, Y. Tang, and K. Wang, "Stability design of single-loop voltage control with enhanced dynamic for voltage-source converters with a low LC-resonant-frequency," *IEEE Trans. Power Electron*., vol. 33, no. 11, pp. 9937–9951, Nov. 2018.

[12] J. Wang, L. Chen, Z. Liu, Z. Zhang and X. Zhang, "Optimized parameter design of the dual-loop control for grid-forming VSCs with LC filters," *IEEE Trans. Ind. Appl*, vol. 58, no. 1, pp. 820-829, Jan.-Feb. 2022.

[13] T. Qoria, F. Gruson, F. Colas, X. Guillaud, M.-S. Debry, and T. Prevos, "Tuning of cascaded controllers for robust grid-forming voltage source converter," in *Proc. PSCC*, 2018, pp. 1–7.

[14] H. Deng, J. Fang, Y. Qi, Y. Tang, and V. Debusschere, "A generic voltage control for grid-forming converters with improved power loop dynamics," *IEEE Trans. Ind. Electron*., vol. 70, no. 4, pp. 3933–3943, Apr. 2023.

[15] A. Akhavan, J. C. Vasquez, and J. M. Guerrero, "Passivity-based control of single-loop grid-forming inverters," *IEEE J. Emerg. Sel. Top. Power Electron*, vol. 4, no. 2, pp. 571-579, April 2023.

[16] A. Akhavan, S. Golestan, J. Vasquez, and J. Guerrero, "Passivity enhancement of voltage-controlled inverters in grid-connected microgrids considering negative aspects of control delay and grid impedance variations," *IEEE J. Emerg. Sel. Topics Power Electron*., vol. 9, no. 6, pp. 6637–6649, Dec. 2021.

[17] X. Li, C. Chen, Y. Sun, and H. Cheng, "Low/middle-frequency positive external-damping design under self-stability constraint for inner control loop of grid-forming converters," *IEEE Trans. Ind. Electron*., vol. 71, no. 5, pp. 4762-4772, May 2024.

[18] H. Yu, M. Awal, H. Tu, Y. Du, S. Lukic, and I. Husain, "Passivity-oriented discrete-time voltage controller design for grid-forming inverters," *Proc. IEEE ECCE*, pp. 469-475, 2019.

[19] H. Wu and X. Wang, "Passivity-based dual-loop vector voltage and current control for grid-forming VSCs," *IEEE Trans. Power Electron*., vol. 36, no. 8, pp. 8647–8652, Aug. 2021.

[20] N. Baeckeland, D. Chatterjee, M. Lu, B. Johnson and G. S. Seo, "Overcurrent limiting in grid-forming inverters: a comprehensive review and discussion," *IEEE Trans. Power Electron, early access*, 2024.

[21] Y. Huang, C. Xie, C. Peng, D. Zhou, and J. Zou, "Rethink and design of capacitor-current-feedback active damping for grid-following inverters from a passivity enhancement perspective," *IEEE J. Emerg. Sel. Top. Power Electron*., vol. 12, no. 3, pp. 2947-2959, June 2024.

[22] R. Cvetanovic, I. Z. Petric, P. Mattavelli, and S. Buso, "Accurate highfrequency modeling of the input admittance of PWM grid-connected VSCs," *IEEE Trans. Power Electron*., vol. 37, no. 9, pp. 10534–10545, Sep. 2022.

[23] S. He, D. Zhou, X. Wang, Z. Zhao, and F. Blaabjerg, "A review of multisampling techniques in power electronics applications," *IEEE Trans. Power Electron*., vol. 37, no. 9, pp. 10514–10533, Sep. 2022.

[24] I. Petric, P. Mattavelli, and S. Buso, "Multi-sampled grid-connected VSCs: A path towards inherent admittance passivity," *IEEE Trans. Power Electron.*, vol. 37, no. 7, pp. 7675–7687, Jul. 2022.

[25] S. He, Z. Yang, D. Zhou, X. Wang, R. W. De Doncker, and F. Blaabjerg, "Dissipativity robustness enhancement for LCL-filtered grid-connected VSCs with multisampled grid-side current control," *IEEE Trans. Power Electron.*, vol. 38, no. 3, pp. 3992–4004, Mar. 2023.

[26] Z. Yang, S. He, D. Zhou, X. Wang, R. De Doncker, F. Blaabjerg, and L. Ding, "Wideband dissipativity enhancement for grid-following VSC utilizing capacitor voltage feedforward," *IEEE J. Emerg. Sel. Top. Power Electron.*, vol. 11, no. 33, pp. 3138-3151, June 2023.

[27] M. Ravanji, D. Rathnayake, M. Mansour, and B. Bahrani, "Impact of voltage-loop feedforward terms on the stability of grid-forming inverters and remedial actions," *IEEE Trans. Energy Convers.*, vol. 38, no. 3, pp. 1554-1565, Sept.2023.

Shan He (IEEE Senior Member) received the B.S. from Northeast Electric Power University, Jilin, China, in 2015, the M.S. degree from Zhejiang University, Hangzhou, China, in 2018, and the Ph.D. from Aalborg University, Aalborg, Denmark, in 2022, all in electrical engineering.

Since 2022, he has been with the Department of Energy Technology, Aalborg University, where he is currently working as a Postdoc. In 2021 and 2023, he was a visiting researcher at RWTH Aachen University and a research associate at Kiel University in Germany, respectively. His research interests include converter control, renewable energy systems, power to x, and battery management.

He has published more than 60 technical papers and 1 book chapter and received 4 conference awards. He serves as the Associate editor of Protection and Control of Modern Power Systems and the session chair in several IEEE conferences.

Chao Gao received the B.S. degree from Wuhan University, Wuhan, China, in 2018, the M.S. degree from Huazhong University of Science and Technology, Wuhan, China, in 2021, and the Ph.D. from the Chinese University of Hong Kong, Hong Kong, China, in 2024, all in electrical engineering. He was a visiting researcher with the department of energy, Aalborg University, Aalborg, Denmark from 2023 to 2024. His research interests include modeling and control of power electronic converters.

Zhiqing Yang (IEEE Member) received the B.S. degree from Southwest Jiaotong University, Chengdu, China, in 2013, and the M.S. and Dr.-Ing. degrees from RWTH Aachen University, Aachen, Germany, in 2017 and 2021, respectively, all in electrical engineering.

From April 2016 to September 2016, he was a Research Intern with the Advanced Technology R&D Center, Mitsubishi Electric, Amagasaki, Japan. From October 2017 to September 2021, he was a Research Associate with the Institute for Power Generation and Storage Systems, RWTH Aachen University. Since January 2022, he has been with the School of Electrical Engineering and Automation, Hefei University of Technology, Hefei, China, as an Associate Professor. His research interests include power electronics in renewable generations and electric vehicles and pules power systems.

Dr. Yang Serves as a Guest AE for CPSS Transactions on Power Electronics and Applications.

Helong Li (Senior Member, IEEE) received the B.Sc. and M.Sc. degrees in electrical engineering from Harbin Institute of Technology, Harbi, China, in 2010 and 2012, respectively, and the Ph.D. degree in electrical engineering from Aalborg University, Aalborg, Denmark, in 2015.

From 2016 to 2019, he worked with Dynex Semiconductor Ltd, as a Senior and Principal R&D Engineer, for power semiconductor packaging, testing, reliability. From 2019 to 2021, he worked with CREE Europe GmbH in the field of SiC automotive applications. Since 2021, he has been with Hefei University of Technology, Hefei, China, as a Professor, focusing on power semiconductor packaging and applications. He authored or coauthored more than 50 scientific papers, and participated in the definition of automotive standard AQG324 for SiC power modules.

Dr. Li was the recipient of Distinguished Young Scholars of the National Natural Science Foundation of China (Overseas) in 2022 and Hubing Scholar from Hefei University of Technology in 2022. He serves as a Guest EiC for IEEE Open Journal of Power Electronics.

Lijian Ding (Member, IEEE) received the B.S. and the M.S. degrees in electrical materials and insulation technology from the Harbin Institute of Electrical Engineering, Harbin, China, in 1992 and 1995, respectively, the Ph.D. degree in theory and new technology of electrical engineering from the North China Electric Power University, Beijing, China, in 2000.

In 2018, he was with the School of Electrical Engineering and Automation, Hefei University of Technology (HFUT), Hefei, China, where he is the Dean and a Full Professor. He also leads the Institute of Energy, Hefei Comprehensive National Science Center. From 2022, he is the Vice President with HFUT. His research interests include high-voltage technology and fault identification, EMC, and reliability of wide bandgap semiconductors and power electronic systems.

Prof. Ding is the recipient of the 2006 Education Ministry's New Century Excellent Talents Award, 2009 China Youth Science and Technology Award, and 2015 National Hundred Million Talents Project Award.

Frede Blaabjerg (IEEE Fellow) received the Ph.D. degree in electrical engineering from Aalborg University, Aalborg, Denmark, in 1995, and the honoris causa degrees from the Universitatae Politehnica Timisoara, Timisoara, Romania, and TalTech—Tallinn University of Technology, Tallinn, Estonia, in 2017 and 2018, respectively.

He was with ABB-Scandia, Randers, Denmark, from 1987 to 1988. In 1992, he became an Assistant Professor with Aalborg University, an Associate Professor in 1996, and a Full Professor of power electronics and drives in 1998, where he has been a Villum Investigator since 2017. He has authored or coauthored more than 600 journal papers in the fields of power electronics and its applications. He has coauthored four monographs and edited ten books in power electronics and its applications. His current research interests include power electronics and its applications, such as in wind turbines, PV systems, reliability, harmonics, and adjustable speed drives.

Dr. Blaabjerg was a Distinguished Lecturer of the IEEE Power Electronics Society from 2005 to 2007 and for the IEEE Industry Applications Society from 2010 to 2011 and from 2017 to 2018. He served as the President of the IEEE Power Electronics Society from 2019 to 2020. He has been the Vice President of the Danish Academy of Technical Sciences. He has received 33 IEEE prize paper awards, the IEEE PELS Distinguished Service Award in 2009, the EPE-PEMC Council Award in 2010, the IEEE William E. Newell Power Electronics Award in 2014, the Villum Kann Rasmussen Research Award in 2014, the Global Energy Prize in 2019, and the 2020 IEEE Edison Medal. He was the Editor-in-Chief of the IEEE TRANSACTIONS ON POWER ELECTRONICS from 2006 to 2012. He was nominated by Thomson Reuters to be among the most 250 cited researchers in engineering in the world for 2014–2020.